RESEARCH ARTICLE

Error assessment and correction for extrusion-based bioprinting using computer vision method

Changxi Liu[1,2], Chengliang Yang[2,3], Jia Liu[2,3]*, Yujin Tang[2,3]*, Zhengjie Lin[4], Long Li[5], Hai Liang[5], Weijie Lu[1,2], Liqiang Wang[1,2]*

[1]State Key Laboratory of Metal Matrix Composites, School of Material Science and Engineering, Shanghai Jiao Tong University, Shanghai, 200240, China

[2]National Center for Translational Medicine, Shanghai Jiao Tong University, Shanghai 200240, China

[3]Department of Orthopaedics, Affiliated Hospital of Youjiang Medical University for Nationalities, Guangxi Key Laboratory of Basic and Translational Research of Bone and Joint Degenerative Diseases, Baise, 533000, Guangxi, China

[4]3D Printing Clinical Translational and Regenerative Medicine Center, Shenzhen Shekou People's Hospital, Shenzhen, 518060, China

[5]Department of Stomatology, Shenzhen Shekou People's Hospital, Shenzhen, 518060, China

(This article belongs to the *Special Issue: Related to 3D printing technology and materials*)

*Corresponding authors:
Jia Liu (liujia@ymcn.edu.cn)
Yujin Tang (tangyujin@ymcn.edu.cn)
Liqiang Wang
(wang_liqiang@sjtu.edu.cn)

Abstract

Bioprinting offers a new approach to addressing the organ shortage crisis. Despite recent technological advances, insufficient printing resolution continues to be one of the reasons that impede the development of bioprinting. Normally, machine axes movement cannot be reliably used to predict material placement, and the printing path tends to deviate from the predetermined designed reference trajectory in varying degrees. Therefore, a computer vision-based method was proposed in this study to correct trajectory deviation and improve printing accuracy. The image algorithm calculated the deviation between the printed trajectory and the reference trajectory to generate an error vector. Furthermore, the axes trajectory was modified according to the normal vector approach in the second printing to compensate for the deviation error. The highest correction efficiency that could be achieved was 91%. More significantly, we discovered that the correction results, for the first time, were in a normal distribution instead of a random distribution.

***Keywords**:* Bioprinting; Computer vision; Error detection; Sobel operator

1. Introduction

Organ shortage is a serious social health crisis. A report from the University of Minnesota states that approximately 90,000 people require kidney transplant, but only 1,500 people have undergone kidney transplants in 2018[1]. The shortage of fitting and propitious organs for transplantation has always been a medical concern[2-4]. Building organs from scratch to explore entirely new cell configurations is the main feature of bioprinting, which is an emerging scientific field that has potential to solve this organ shortage crisis[5,6].
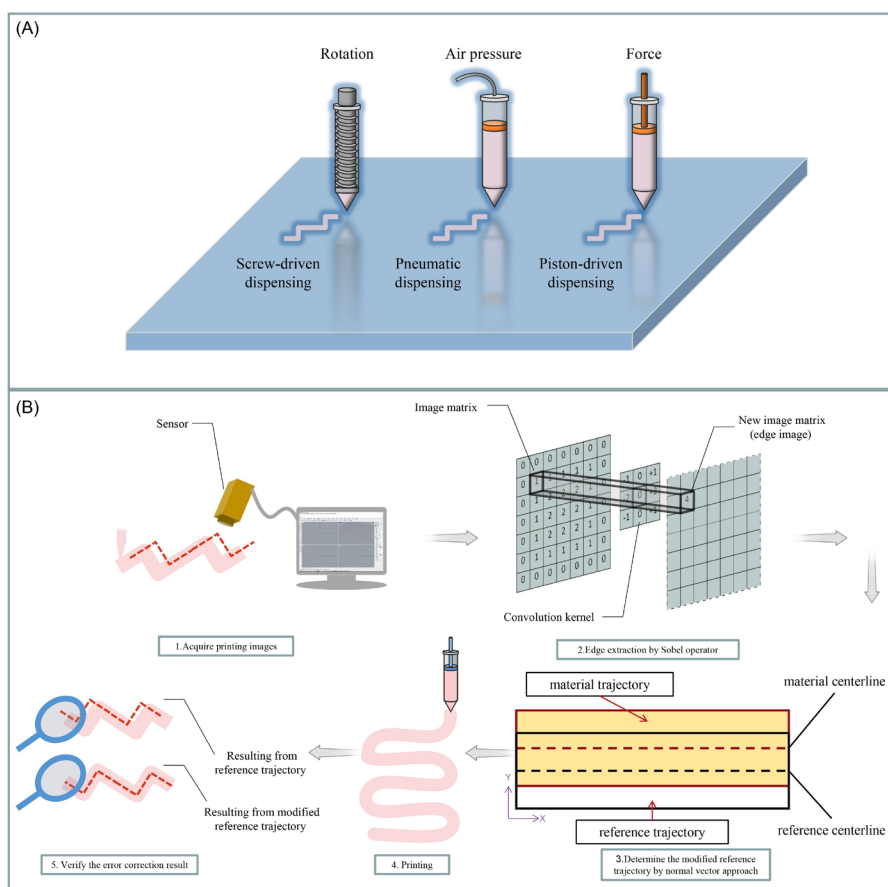
Figure 1. (A) A schematic diagram demonstrating the power source of extrusion-based bioprinting. From left to right, the schematic shows screw-driven dispensing, pneumatic dispensing, and piston-driven dispensing. (B) Examples for identifying and correcting errors based on computer vision. The Sobel operator is used to obtain the original printing error, and a complete correction plan is prepared using the normal vector approach.

At present, the research field of bioprinting includes scaffold fabrication[7,8], organ-on-a-chip manufacturing[9], tissue repair[10], and toxicity testing[11,12]. Building patient-specific organs to alleviate organ shortages remains a major challenge in the bioprinting field[13-15].

Bioprinting methods can be divided into inkjet-based, laser-based, extrusion-based, and stereolithography-based bioprinting[15]. Compared with other printing methods, extrusion-based bioprinting is the most often used, as it has high throughput and a fast printing speed[16-18]. Extrusion-based bioprinting mainly relies on rotation dispensing, air pressure dispensing, or force dispensing, as shown in Figure 1A.

Although extrusion-based bioprinting has more advantages compared to other printing methods, the low printing resolution is the main reason that limits the advancement of extrusion-based bioprinting in various fields[19-22]. Moreover, many studies have pointed out that resolution is an important parameter for bioprinting; for instance, a study on artificially printing human heart pointed out that high resolution is an important requirement for stable manufacturing of the heart[23]. Hence, it is necessary to emphasize and improve on the resolution of extrusion-based bioprinting.

The defect in the deviation of the actual printing path from the predetermined path, and the deviation error value that remains in the final printed organ are the main reasons for the low resolution of extrusion-based bioprinting[24,25]. Normally, the deviation value between the reference path and the printing path is small in linear shape areas; however, the deviation error shows a significant increasing tendency when the path changes to a curved shape. The whole helix is composed of the antihelix and helix, which is a curved structure that has been printed in many studies. However, the research on helix printing still lacks a method that can precisely control the printing path and reduce the deviation error value between the printing path and the reference path; moreover, there is still much room for improvement in terms of printing resolution[26,27].
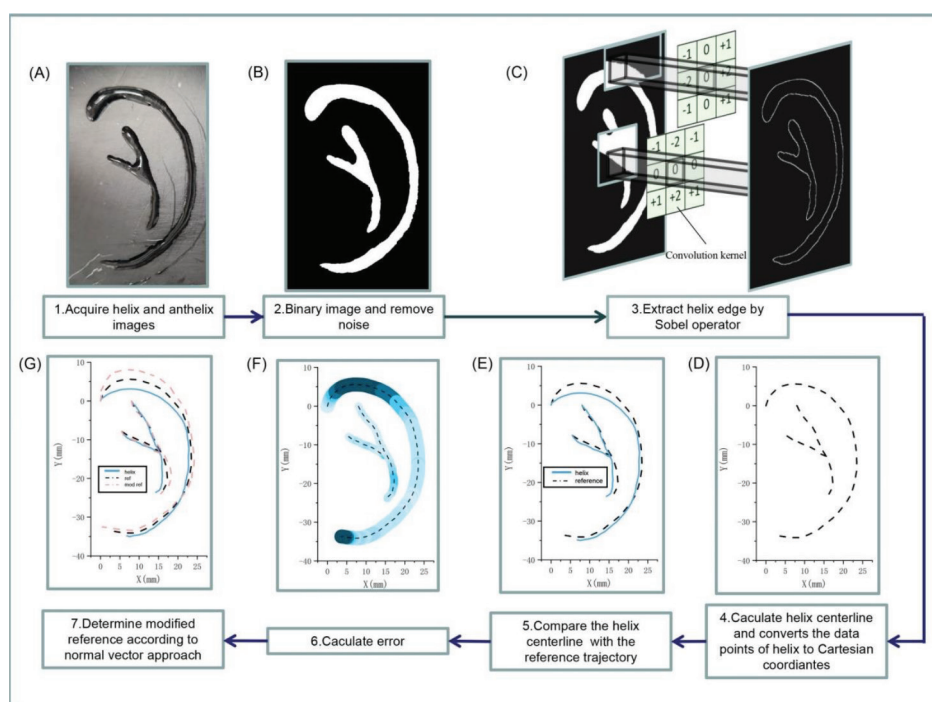
Figure 2. (A-C) The image data is converted into point cloud data after binarization and centerline calculation according to the Sobel operator. (D-G) Additional error information and modified reference path information are calculated based on the centerline.

This research focuses on the complex antihelix and helix structure using the Sobel operator and the normal vector approach to reduce the printing error to an acceptable range, thus improving the printing resolution (Figure 1B). A process control method based on computer vision was used in this study to enable the detection and correction of the path errors of the antihelix and helix. Furthermore, the deviation error was controlled to an acceptable range to ensure that the accuracy of the helix printing path shows an increasing tendency.

2. Methods

2.1. Equipment
Based on the initial bioprinting machine, a non-contact camera was placed above the printing platform to capture the path of the antihelix and helix after printing. The non-contact camera covered a range of 40 mm × 40 mm rectangle to ensure that the complete helix could be captured.

Two different antihelix and helix structures were designed and counted in this study. Each helix structure had different antihelix and helix. The purpose of counting the two helix groups was to determine the difference in error values carried by different shapes of helices and prove that the correction methods are universal.

2.2. Bioinks
An alginate-based hydrogel system for applications in bioink was selected for bioprinting helix[28-30]. The alginate-

based hydrogel has excellent mechanical and biological properties, and it is widely used in tissue engineering, including drug delivery[31], vaccine manufacturing[32], tissue regeneration[33], and bioprinting[34].

2.3. Image algorithm
Since the captured image cannot be directly recognized by the correction algorithm, the helix image needs to be pre-processed. Figure 2 illustrates in detail how abstract image data is converted into spatial point cloud data to be recognized by the correction algorithm. The first step involves acquiring the antihelix and helix images through a non-contact camera placed above the printing platform. Through binarization processing, the image matrix is reduced from three channels to a single channel, and the gray value in the image matrix is only 0 or 255; additionally, noise is also removed. The purpose of this step is to enhance the contour features of the helix and prepare for the next step. In the third step, a computer vision-based method is used to extract the edges of the helix printing image. The Sobel operator is widely used in image edge detection and extraction due to its fast response and high precision. The Sobel operator usually consists of two 3 × 3 convolution kernels. The two convolution kernels would respond the most to the horizontal edge and the vertical edge, respectively. Following the processing of pixels in the image matrix by convolution, the Sobel operator outputs two images with a horizontal edge and a vertical edge, and
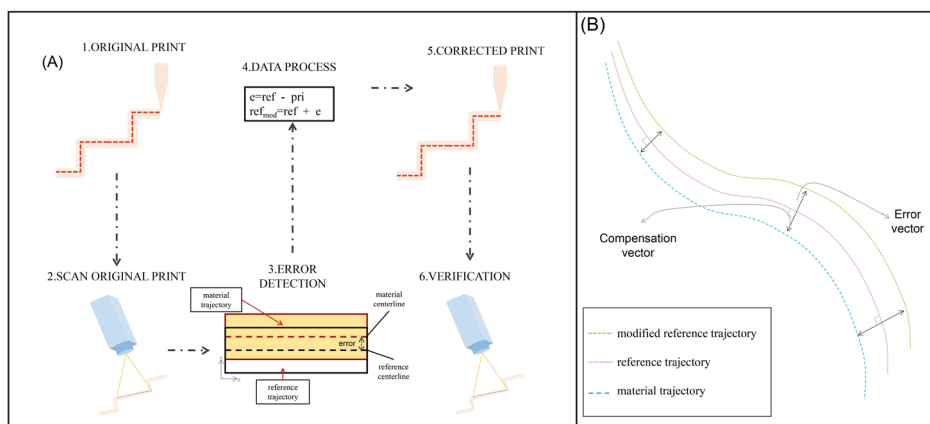
Figure 3. A schematic illustration of the process and algorithm of helix printing error detection and correction. (A) Six steps of helix error detection and correction in bioprinting. (B) Explanation of the normal vector approach: a compensation vector is added based on the reference path to obtain the modified reference path, the size of which is the same as the error vector, but in opposite direction.

after the two images are superimposed, the whole helix edge is extracted[35-37].

In the fourth step, the estimated value of the helix centerline is calculated and defined as the spatial path of the printed helix. In the fifth step, the point cloud data of the estimated helix centerline and the coordinate data of the reference path are placed in the same Cartesian coordinate system for comparison and calculation of the error between the two trajectories. In the sixth step, the error vector between the printing path and the reference path is calculated, and the error is mapped onto the printing path through different shades of color. The specific calculation method will be discussed in detail in the next section. In the seventh step, the modified reference path is obtained by a compensation vector based on the original reference path. Figure 2G shows the helix printing path (blue solid line), original reference path (black dashed line), and modified reference path (red dashed line).

2.4. Correction algorithm

Considering that the accuracy of the helix path is affected by the mechanical axes movement, it would be an effective attempt to adjust and control the print head to compensate for errors in the printing process. The entire automated correction algorithm can be divided into the error detection part and the execution operation part, as shown in Figure 3A. In the error detection part, the deviation errors between the helix printing path and the reference path are calculated, and these errors are automatically collected to modify the reference path by compensation vector to reduce the offset value of the helix path.

The first step involves the original printing, in which the material is extruded from the print head according to the reference path without any additional operations. The deviation error value between the printing path and the reference path is fully retained in this step. The second step involves obtaining the point cloud data of the original helix printing path. Generally, the collected printed helix image cannot be recognized by the correction algorithm. Therefore, the Sobel operator is used to extract the edge of the helix printing image. Then, the centerline of the helix is calculated to represent the real-space position coordinates. The specific details of point cloud conversion have been discussed in section 2.3.

The third and fourth steps involve detecting the deviation error between the original helix printing path and the reference path as well as calculating the modified reference path. Based on Figure 3B, the normal vector approach determines the compensation vector by taking the mirror image of the error vector to the reference path. The magnitude of the compensation vector is equal to that of the error vector, but in an opposite direction. Furthermore, the modified reference path is calculated based on the compensation vector added to the original reference path.

In the fifth step, the helix printing path is a result of the modified reference path, which is different from the original reference path in the first step. In the sixth step, the deviation error value between the new helix path, resulting from the modified reference path, and the reference path is recollected. Finally, the helix printing image is recollected in the fifth step. Similar to the second step, the image processing algorithm, as discussed in section 2.3, converts the helix image data into point cloud data.

3. Results

3.1. Original printing

The printing data of the original helix was successfully counted in the Cartesian coordinate system using the
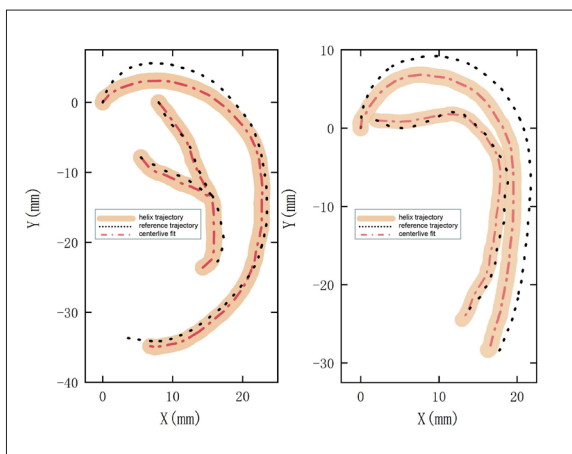
Figure 4. The helix and antihelix printing trajectory data points (flesh-colored solid), the as-designed reference trajectory (black dash line), and the centerline of the printing trajectory (red dotted line). The centerline reflects the printing trajectory of the material in the joint space.

computer vision-based image method (Figure 4). The actual helix printing path deviated from the as-designed reference path, thus necessitating additional supervision. The flesh-colored path represents the helix and antihelix printing path, while the black dashed line represents the reference path; the red dotted line represents the centerline of the helix and antihelix path, which reflects the coordinate position of the printing path and facilitates the calculation of the deviation value from the reference path.

3.2. Correct printing

Through computer vision-based algorithm processing, the accuracy of the two helix trajectories improved significantly. Figure 5 illustrates the helix and antihelix printing path resulting from the modified reference path and the original reference path to compare the correction effects. The white path represents the original helix and antihelix printing path, the transparent blue path represents the printing path resulting from the modified reference path, while the black double-dotted line represents the as-designed reference path.

The original reference path, modified reference path, original helix and antihelix printing path, as well as the new helix and antihelix printing path were analyzed and compared in Figure 6. The topmost figures show the as-designed original reference path and the modified reference path with the compensation vector. The black dashed line represents the original reference path, while the blue solid line represents the modified reference path. The bottom figures show the helix and antihelix printing path resulting from the modified reference path, which is closer to the as-designed reference path than the original helix and antihelix printing path. The blue solid line represents the helix and antihelix path resulting from the original reference path, the red dotted line represents the helix
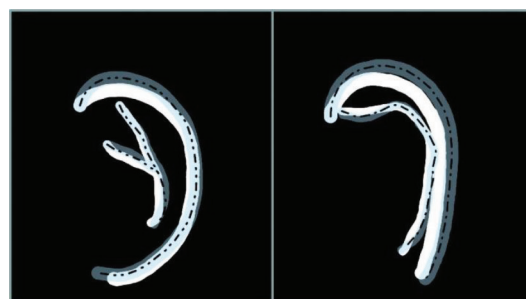

Figure 5. Image overlay of the fabrication helix at different stages to detect the correction effect for each helix. The white path represents the original path, the transparent blue path represents the corrected path, and the black dotted line represents the as-designed reference path.
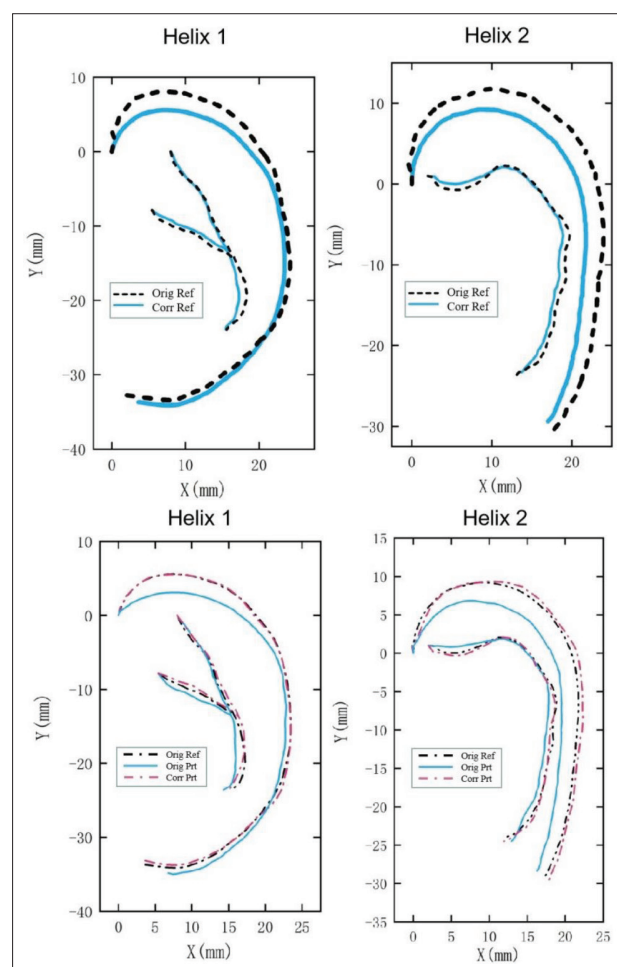

Figure 6. Top: comparison of the modified reference path (blue solid line, Corr Ref), used to fabricate the Corrected Print, with the original reference path (black dash line, Orig Ref), used to fabricate the Original Print. Bottom: comparison of the original fabrication path (blue solid line, Orig Prt), resulting from reference path, with the corrected fabrication path (pink dotted line, Corr Prt).

and antihelix printing path resulting from the modified reference path, and the black dotted line represents the original reference path.
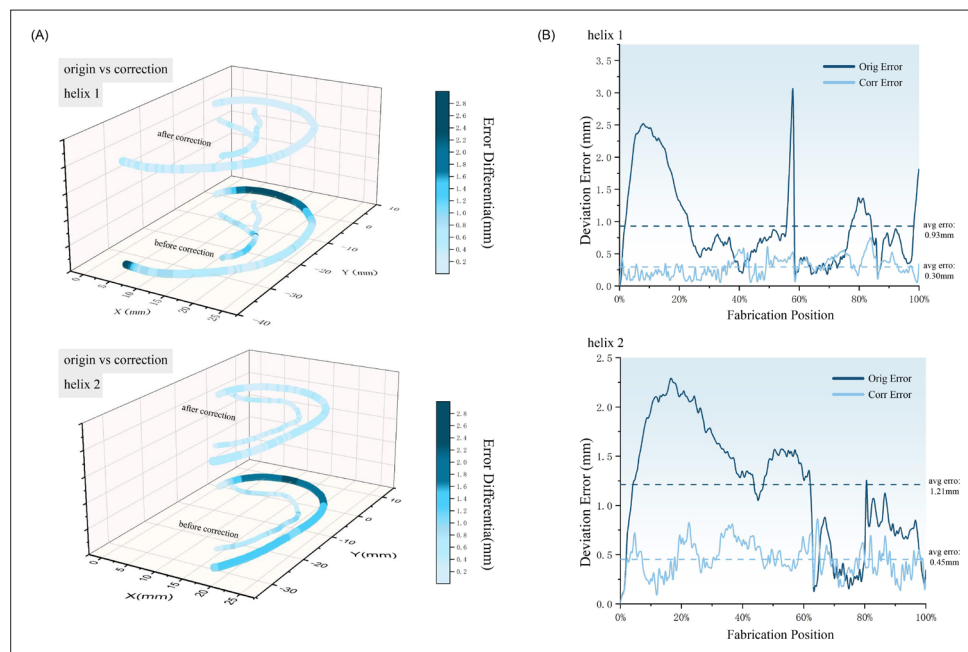
Figure 7. The figure illustrates the error carried by the original fabrication and corrected fabrication. (A) The magnitude of error of the original and corrected fabrication helix on the reference path is represented by the shade of color of the path. The error bar on the right shows that the magnitude of error increases as the shade of color changes from light to dark blue. (B) All original fabrication and corrected fabrication errors are recorded for each helix. The abscissa reflects each position of fabrication. Dark blue represents the original fabrication, while light blue represents the corrected fabrication.

Combined with the training of the error vector, the compensation vector was added to the original reference path to obtain a modified reference path that would result in a better position with less printing errors. Figure 7A illustrates the magnitude of error carried by the helix and antihelix before and after correction. The different shades of color surrounding the helix and antihelix represent the magnitude of error of the area; the magnitude of error changes from small to large as the color transitions from light to dark. The helix and antihelix path on top resulted from the modified reference path, while the one at the bottom resulted from the original reference path. The error bar on the right reflects the error magnitude corresponding to the shade of color surrounding the helix and antihelix. Figure 7B records the error carried by each position for the two helices.

4. Discussion

There are relatively few studies on reducing printing deviation errors to improve the resolution of bioprinting. Considering that the deviation error value in actual printing might be difficult to perceive with the naked eye, a novel correction control system based on computer vision was designed and used in this study to realize the identification and correction of small errors. The final quality of the helix can be improved by adjusting the reference trajectories for the helix and antihelix. There was a significant reduction in

the deviation error value of the path following the addition of the computer vision-based control. This indicates that the accuracy and resolution of bioprinting have risen by a level.

Figure 8 illustrates the correction results of the helix and antihelix after correction algorithm training. Original printing error existed in each range, and the error was randomly distributed as shown in the figure. Without correction control, the print heads deviated from the predetermined path in different positions. For the position where multi-axis coordinated motion is required, the error will show an increasing tendency. For single-axis motion position, the error carried will show a decreasing tendency. With the addition of the compensation vector to the reference path, the error distribution fell in the low error range on the left. More significantly, the error distribution was in a normal distribution instead of a random distribution. This shows that the correction method based on computer vision control has the same and efficient effect on different areas.

Before the correction, most areas of the helix path deviated from the as-designed reference path, and the distance between the two trajectories was significant (Figure 6). After image algorithm training, the distance between the helix path and reference path reduced significantly, and most of the areas overlapped. This shows that the computer vision-based method plays a significant role in path guidance.
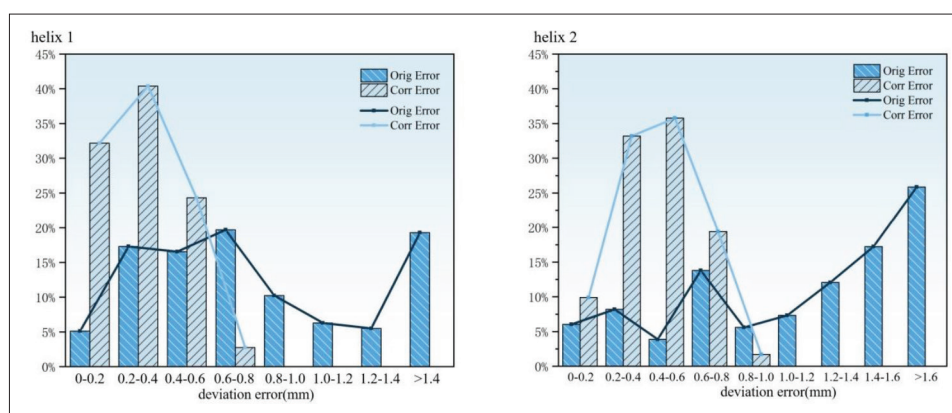
Figure 8. The deviation errors of different ranges are counted for the original printing and the corrected printing. The ordinate indicates the percentage of error in a certain range to the total error.

Furthermore, the modified helix path of the printing part was compared to the path of the as-designed model to compute the printing accuracy, which was defined as the average deviation error of different areas. The deviation error value between the helix printing point cloud data and the reference path was calculated based on the Euclidean norm (1), which is different for each area. For each helix, the dark blue area concentrated at the turning of the helix at the top suggests that the curve path is the area with the largest deviation from the as-designed reference path, with a maximum error of 2.47 mm (Figure 7A). On the other side, the antihelix and other helix areas rely on less curved structures, in which the shade is lighter than the area at the top of the helix and located in the medium error range. The phenomenon of high error at the curved area and low error at the straight line area is consistent with that described by other researchers[25,38].

$$\|x_2\| = \sqrt{\sum_{i=1}^{N} x_i^2} \tag{1}$$

The high error and medium error areas in the helix path improved significantly after algorithm training. The error after correction was in the light blue low error area, which was less than the deviation value of 1 mm. The average error value of the two helices reduced from 0.93 mm and 1.21 mm to 0.30 mm and 0.45 mm, respectively. Moreover, the average value of the high error area dropped from 2.41 mm and 2.16 mm to 0.21 mm and 0.31 mm, respectively, whereas the average value of the medium error area dropped from 1.29 mm and 1.55 mm to 0.25 mm and 0.38 mm, respectively, for each helix (Figure 7). The correction efficiency of the high error area reached 91% and 85%, while that of the medium error area reached 80% and 75%. This result shows that the normal vector approach exhibits a strong correction ability in improving material placement and has a consistent correction effect for different error areas.

A breakthrough has been made in the modification strategy for trajectory correction, in which the deviation error between the reference path and the printing path has been reduced to an acceptable range. Researchers should attempt to further probe into the accuracy of the complete ear trajectory in the entire printing space. The definition of trajectory deviation error has also been transformed from two-dimensional space to three-dimensional space. However, various challenges exist in this work. Although point cloud data collection in two-dimensional space based on computer vision shows superior performance, the limitations of computer vision are magnified in two-dimensional cloud data collection. Furthermore, error definition would also shift from two-dimensional space to three-dimensional space. Hence, further investigations are required in this field of research.

The conversion of image data into component point cloud data is an important step to achieve path correction. With accurate trajectory point cloud data, it is feasible to accurately describe and define the position coordinates of components in real space. With the advancement of computer science, computer vision algorithms with powerful processing capabilities in image processing would be uncovered, allowing the edges of printed components to be extracted more accurately[39].

5. Conclusion

We added a computer vision-based method to this study to improve the bioprinting resolution and printing accuracy. The error between the helix printing path and the reference path is one of the main reasons that limits the printing resolution. The path error was defined through the image algorithm, and the original reference path was modified for the second printing. The error of the helix printing path resulting from the modified reference path was reduced

to an acceptable range. This method showed a significant reduction effect for high error areas. More importantly, the error of the correction results was in a normal distribution instead of a random distribution, thus proving that this method based on computer vision is universal for different locations.

This research has demonstrated a method for effectively detecting defects and correcting errors in the field of bioprinting. In fact, this method is also suitable for improving the resolution of printing other organs. We hope that bioprinting can further advance and create new opportunities for regenerative medicine.

Acknowledgments

Funding

Author contributions

Conceptualization: Changxi Liu, Liqiang Wang
Data curation: Changxi Liu, Chengliang Yang, Jia Liu
Funding acquisition: Yujin Tang, Zhengjie Lin, Long Li, Hai Liang
Methodology: Changxi Liu, Weijie Lu
Writing – original draft: Changxi Liu, Jia Liu, Yujin Tang, Hai Liang, Weijie Lu, Liqiang Wang
Writing – review & editing: Changxi Liu, Jia Liu, Yujin Tang, Hai Liang, Weijie Lu, Liqiang Wang

Ethics approval and consent to participate

Not applicable.

Consent for publication

Not applicable.

Availability of data

Experimental data are measured and analyzed by computer.

References

1. Hart A, Smith JM, Skeans MA, *et al.*, 2020, OPTN/SRTR 2018 annual data report: Kidney. *Am J Transplant*, 20(s1): 20–130.

   https://doi.org/10.1111/ajt.15672

2. Abouna GM, 2008, Organ shortage crisis: Problems and possible solutions. *Transplant Proc*, 40(1): 34–38.

   https://doi.org/10.1016/j.transproceed.2007.11.067

3. Croome KP, Lee DD, Keaveny AP, *et al.*, 2017, Noneligible donors as a strategy to decrease the organ shortage. *Am J Transplant*, 17(6): 1649–1655.

   https://doi.org/10.1111/ajt.14163

4. Bastani B, 2020, The present and future of transplant organ shortage: Some potential remedies. *J Nephrol*, 33(2): 277–288.

   https://doi.org/10.1007/s40620-019-00634-x

5. Vijayavenkataraman S, Yan WC, Lu WF, *et al.*, 2018, 3D bioprinting of tissues and organs for regenerative medicine. *Adv Drug Deliv Rev*, 132: 296–332.

   https://doi.org/10.1016/j.addr.2018.07.004

6. Pedde RD, Mirani B, Navaei A, *et al.*, 2017, Emerging biofabrication strategies for engineering complex tissue constructs. *Adv Mater*, 29(19): 1–27.

   https://doi.org/10.1002/adma.201606061

7. van Pel DM, Harada K, Song D, *et al.*, 2018, Modelling glioma invasion using 3D bioprinting and scaffold-free 3D culture. *J Cell Commun Signal*, 12(4): 723–730.

   https://doi.org/10.1007/s12079-018-0469-z

8. Liu C, Yang C, Liu J, *et al.*, 2022, Medical high-entropy alloy: Outstanding mechanical properties and superb biological compatibility. *Frontiers in Bioengineering and Biotechnology*, 1436.

   https://doi.org/10.3389/fbioe.2022.952536

9. Yu F, Choudhury D, 2019, Microfluidic bioprinting for organ-on-a-chip models. *Drug Discov Today*, 24(6): 1248–1257.

   https://doi.org/10.1016/j.drudis.2019.03.025

10. Li S, Tian X, Fan J, *et al.*, 2019, Chitosans for tissue repair and organ three-dimensional (3D) bioprinting. *Micromachines*, 10(11): 765.

    https://doi.org/10.3390/mi10110765

11. Tseng H, Gage JA, Shen T, *et al.*, 2015, A spheroid toxicity assay using magnetic 3D bioprinting and real-time mobile device-based imaging. *Sci Rep*, 5: 1–11.

    https://doi.org/10.1038/srep13987

12. Peng W, Datta P, Ayan B, *et al.*, 2017, 3D bioprinting for drug discovery and development in pharmaceutics. *Acta Biomater*, 57: 26–46.

    https://doi.org/10.1016/j.actbio.2017.05.025

13. Daly AC, Prendergast ME, Hughes AJ, *et al.*, 2021, Bioprinting for the biologist. *Cell*, 184(1): 18–32.

    https://doi.org/10.1016/j.cell.2020.12.002

14. Rastogi P, Kandasubramanian B, 2019, Review of alginate-based hydrogel bioprinting for application in tissue engineering. *Biofabrication*, 11(4): 042001.

    https://doi.org/10.1088/1758-5090/ab331e

15. Jose RR, Rodriguez MJ, Dixon TA, *et al.*, 2016, Evolution of bioinks and additive manufacturing technologies for 3D bioprinting. *ACS Biomater Sci Eng*, 2(10): 1662–1678.

    https://doi.org/10.1021/acsbiomaterials.6b00088

16. Ozbolat IT, Hospodiuk M, 2016, Current advances and future perspectives in extrusion-based bioprinting. *Biomaterials*, 76: 321–343.

    https://doi.org/10.1016/j.biomaterials.2015.10.076

17. Paxton N, Smolan W, Böck T, *et al.*, 2017, Proposal to assess printability of bioinks for extrusion-based bioprinting and evaluation of rheological properties governing bioprintability. *Biofabrication*, 9(4): 044107.

    https://doi.org/10.1088/1758-5090/aa8dd8

18. Chung JHY, Naficy S, Yue Z, *et al.*, 2013, Bio-ink properties and printability for extrusion printing living cells. *Biomater Sci*, 1(7): 763–773.

    https://doi.org/10.1039/c3bm00012e

19. Blaeser A, Duarte Campos DF, Puster U, *et al.*, Controlling shear stress in 3D bioprinting is a key factor to balance printing resolution and stem cell integrity. *Adv Healthc Mater*, 5(3): 326–333.

    https://doi.org/10.1002/adhm.201500677

20. Lee JM, Ng WL, Yeong WY, 2019, Resolution and shape in bioprinting: Strategizing towards complex tissue and organ printing. *Appl Phys Rev*, 6(1): 011307.

    https://doi.org/10.1063/1.5053909

21. Suntornnond R, Tan EYS, An J, *et al.*, 2016, A mathematical model on the resolution of extrusion bioprinting for the development of new bioinks. *Materials (Basel)*, 9(9): 756.

    https://doi.org/10.3390/ma9090756

22. Wang Z, Abdulla R, Parker B, *et al.*, 2015, A simple and high-resolution stereolithography-based 3D bioprinting system using visible light crosslinkable bioinks. *Biofabrication*, 7(4): 45009.

    https://doi.org/10.1088/1758-5090/7/4/045009

23. Lee A, Hudson AR, Shiwarski DJ, *et al.*, 2019, 3D bioprinting of collagen to rebuild components of the human heart. *Science (80-.)*, 365(6452): 482–487.

    https://doi.org/10.1126/science.aav9051

24. Bertassoni LE, Cardoso JC, Manoharan V, *et al.*, 2014, Direct-write bioprinting of cell-laden methacrylated gelatin hydrogels. *Biofabrication*, 6(2): 024105.

    https://doi.org/10.1088/1758-5082/6/2/024105

25. Armstrong AA, Alleyne AG, Wagoner Johnson AJ, 2020, 1D and 2D error assessment and correction for extrusion-based bioprinting using process sensing and control strategies. *Biofabrication*, 12(4): 045023.

    https://doi.org/10.1088/1758-5090/aba8ee

26. Armstrong AA, Pfeil A, Alleyne AG, *et al.*, 2021, Process monitoring and control strategies in extrusion-based bioprinting to fabricate spatially graded structures. *Bioprinting*, 21(September 2020): e00126.

    https://doi.org/10.1016/j.bprint.2020.e00126

27. Liu C, Liu J, Yang C, *et al.*, 2022, Computer vision-aided 2D error assessment and correction for helix bioprinting. *Int J Bioprinting*, 8(2): 174–186.

    https://doi.org/10.18063/ijb.v8i2.547

28. Axpe E, Oyen ML, 2016, Applications of alginate-based bioinks in 3D bioprinting. *Int J Mol Sci*, 17(12): 1976.

    https://doi.org/10.3390/ijms17121976

29. Wang B, Wan Y, Zheng Y, *et al.*, 2019, Alginate-based composites for environmental applications: A critical review. *Crit Rev Environ Sci Technol*, 49(4): 318–356.

    https://doi.org/10.1080/10643389.2018.1547621

30. Rastogi P, Kandasubramanian B, 2019, Review of alginate-based hydrogel bioprinting for application in tissue engineering. *Biofabrication*, 11(4): 042001.

    https://doi.org/10.1088/1758-5090/ab331e

31. Jain D, Bar-Shalom D, 2014, Alginate drug delivery systems: Application in context of pharmaceutical and biomedical research. *Drug Dev Ind Pharm*, 40(12): 1576–1584.

    https://doi.org/10.3109/03639045.2014.917657

32. AbdelAllah NH, Gaber Y, Rashed ME, *et al.*, 2020, Alginate-coated chitosan nanoparticles act as effective adjuvant for hepatitis A vaccine in mice. *Int J Biol Macromol*, 152: 904–912.

    https://doi.org/10.1016/j.ijbiomac.2020.02.287

33. Ghosh M, Halperin-Sternfeld M, Grinberg I, *et al.*, 2019, Injectable alginate-peptide composite hydrogel as a scaffold for bone tissue regeneration. *Nanomaterials*, 9(4): 497.

    https://doi.org/10.3390/nano9040497

34. Łabowska MB, Cierluk K, Jankowska AM, *et al.*, 2021, A review on the adaption of alginate-gelatin hydrogels for 3D cultures and bioprinting. *Materials (Basel)*, 14(4): 1–28.

https://doi.org/10.3390/ma14040858

35. Vairalkar MK, 2012, Edge detection of images using Sobel operator. *Int J Emerg Technol Adv Eng*, 2(1): 291–293 [Online]. Available: www.ijetae.com

36. Wang W, 2009, Reach on Sobel operator for vehicle recognition. *2009 International Joint Conference on Artificial Intelligence,* 448–451.

https://doi.org/10.1109/JCAI.2009.54

37. Kanopoulos N, Vasanthavada N, Baker RL, 1988, Design of an image edge detection filter using the Sobel operator. *IEEE J Solid-State Circuits*, 23(2): 358–367.

https://doi.org/10.1109/4.996

38. Armstrong AA, Norato J, Alleyne AG, *et al.*, 2020, Direct process feedback in extrusion-based 3D bioprinting. *Biofabrication*, 12(1): 015017.

https://doi.org/10.1088/1758-5090/ab4d97

39. Liu C, Wang L, Lu W, *et al.*, 2022, Computer vision-aided bioprinting for bone research. *Bone Res*, 10(1): 1–14.

https://doi.org/10.1038/s41413-022-00192-2